

2D Helium Atom Diffraction from a Microscopic Spot

Nick A. von Jeinsen^{1,†,‡}, Sam M. Lambrick^{1,‡}, Matthew Bergin^{2,*}, Aleksandar Radić¹,
Boyao Liu¹, Dan Seremet¹, Andrew P. Jardine¹, and David J. Ward¹

¹*Department of Physics, Cavendish Laboratory, JJ Thomson Avenue, University of Cambridge, Cambridge CB3 0HE, United Kingdom*

²*Centre for Organic Electronics, Physics Building, University of Newcastle, Callaghan, New South Wales 2308, Australia*

 (Received 3 March 2023; revised 1 June 2023; accepted 20 September 2023; published 6 December 2023)

A method for measuring helium atom diffraction with micron-scale spatial resolution is demonstrated in a scanning helium microscope (SHeM) and applied to study a micron-scale spot on the (100) plane of a lithium fluoride (LiF) crystal. The positions of the observed diffraction peaks provide an accurate measurement of the local lattice spacing, while a combination of close-coupled scattering calculations and Monte Carlo ray-tracing simulations reproduce the main variations in diffracted intensity. Subsequently, the diffraction results are used to enhance image contrast by measuring at different points in reciprocal space. The results open up the possibility for using helium microdiffraction to characterize the morphology of delicate or electron-sensitive materials on small scales. These include many fundamentally and technologically important samples which cannot be studied in conventional atom scattering instruments, such as small grain size exfoliated 2D materials, polycrystalline samples, and other surfaces that do not exhibit long-range order.

DOI: [10.1103/PhysRevLett.131.236202](https://doi.org/10.1103/PhysRevLett.131.236202)

Two-dimensional systems including surfaces, single atomic layer materials, and surface localized states are all of current interest due to the unique structural, electronic, and mechanical properties that they can exhibit [1–3]. Examples include the now ubiquitous graphene [4], a multitude of related and layered materials such as hexagonal boron nitride [5] and the transition metal dichalcogenides [6], and topologically protected materials such as bismuth antimonide [7]. To study the structure of such materials, techniques are required that are sensitive to the outermost atomic layer.

However, most surface-sensitive techniques, such as low-energy electron diffraction (LEED) and x-ray photoelectron spectroscopy, face a challenge in their penetration depth of up to about 10 nm. As a result, the substrate or bulk material can dominate the data and make it challenging to detect any adsorbed species, including contaminants. Electron and x-ray-based methods can also deposit large amounts of energy and/or charge in the sample, which can compromise sensitive materials.

Thermal energy atom scattering, usually using < 100 meV helium atoms, provides the ultimate surface sensitive

technique, thus making it ideal for 2D material characterization. Incident helium atoms interact with and scatter from the outermost electrons in the substrate, typically 2–3 Å above the ion cores of the surface atoms [8]. Helium diffraction is ideal for studying structure, and more widely helium scattering is well suited to measuring a range of important material properties [9]. However, until now, helium scattering has been limited to samples with a high degree of uniformity over at least a few millimeters. It has been impossible to study small samples, including many 2D materials produced by exfoliation, or materials used *in situ* within devices. Similar limitations apply to polycrystalline materials, where grain sizes are typically in the micron range, or to other nonuniformities, such as an extended phase change across a surface.

Here, we report the first helium microdiffraction patterns obtained from a highly localized point on a nonuniform surface, using a modified scanning helium microscope (SHeM) [10–15].

SHeM uses a thermal helium beam that has been focused or collimated to micron scales, which enables microscopic imaging. The angular resolution of the instrument was enhanced, and a new measurement scheme was developed, enabling complete LEED-like diffraction patterns to be obtained. Our measurements were performed on lithium fluoride (LiF), which has been studied extensively using thermal-energy, atom-scattering, and grazing-incidence fast-atom diffraction [16,17]. 3D potential energy surfaces, are available that have been obtained by comparison with

Published by the American Physical Society under the terms of the Creative Commons Attribution 4.0 International license. Further distribution of this work must maintain attribution to the author(s) and the published article's title, journal citation, and DOI.

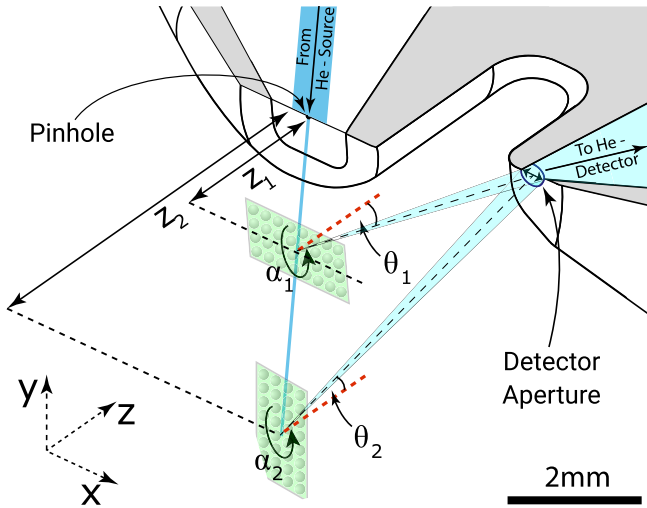


FIG. 1. Schematic of the SHeM scattering geometry, illustrating the presented measurement mode, where the detection angle θ to the sample surface normal (dashed red lines), is varied by changing the distance z from the pinhole. To keep the same spot on the sample illuminated during the variation of θ , it is also translated in the x direction. The sample azimuthal angle α is varied to obtain a complete 2D reciprocal space measurement.

experiment [18–20] which allows the modeling of the results to demonstrate consistency with previous work.

Figure 1 illustrates the core geometry of the Cambridge “A-SHeM” that was used in the current Letter. A broad beam is first produced in a free jet atom source, then is collimated by a fine pinhole to form the helium beam with micron-sized lateral extent incident on the sample. The helium atoms scatter from the surface; those scattered at a specific angle θ pass through the detector aperture into a high-efficiency mass spectrometer [21], the signal from which is used to form each pixels’ intensity.

To obtain diffraction patterns, both polar and sample azimuthal angles must be varied while accurately maintaining constant incidence conditions at a specific spot on the surface. The SHeM is designed for high-resolution imaging, utilizing three linear nanopositioners [22,23] and a rotation stage (additional details can be found in Supplemental Material [24]) [25] to manipulate the sample, but has a fixed detector aperture, so it is not currently possible to directly move the detector. Instead, as illustrated in Fig. 1, the polar angle can be scanned by varying the z position of the sample along the incident beam direction [26]. The motion results in a corresponding change in the detection angle, as shown by the difference between θ_1 and θ_2 in Fig. 1. Variation of the sample azimuthal angle α was achieved by rotating the sample about its normal. Since the center of azimuthal rotation is determined by the sample manipulator, the lateral coordinates of the measurement point needed to be obtained for each azimuthal position. A rotational transformation matrix was used, based on the position of the true center of rotation

(COR) for the stage, in the imaging coordinate system. The coordinates of the COR were determined through the acquisition of a series of calibration images at varying sample azimuthal angles. A detailed description of the method calculating the COR can be found in Appendix A which yielded a maximum error in the tracking of 27 μm . We make an important distinction between the imaging resolution, which is dominated by the helium beam spot size [27] ($\sim 10 \mu\text{m}$) and the accuracy of the point tracking in the current implementation (estimated as $< 27 \mu\text{m}$). An alternative point tracking scheme could allow the study of smaller areas, limited by the beam spot size.

Compared to a typical high-resolution SHeM imaging configuration [28], higher angular resolution was required to resolve distinct diffraction peaks. A detector acceptance angle of $\theta_A \approx 8^\circ$ was implemented, along with a lateral spot size of $R_S \approx 10 \mu\text{m}$, to maintain high signal levels [29]. Such conditions were implemented using a custom “pinhole plate,” that can be manufactured either by conventional machining or 3D printing [30], and employs the geometry shown in Fig. 1 within the wider SHeM instrument.

For elastic scattering at an outgoing angle θ_f , the in-plane momentum transfer is given by

$$\Delta K = k_i(\sin \theta_f - \sin \theta_i), \quad (1)$$

where $\theta_i = 45^\circ$ is the incoming beam angle and $k_i = 2\pi/\lambda$ is the magnitude of the incident helium wave vector.

The intensity can then be measured as it varies with in-plane scattering momentum transfer for each sample azimuth α , by rotating the sample. Note the subtle difference between our approach to measuring the 2D scattering distribution and a typical diffraction measurement with a broad area detector; instead of measuring out-of-plane momenta transfers, we rotate the sample to obtain in-plane scattering at each azimuthal orientation.

2D diffraction scans are plotted by first transforming the collected data from $I(\theta_f, \alpha_{\text{stage}})$ into $I(\Delta K, \alpha)$, using Eq. (1) and a shift in the origin of the α axis to match a principle crystallographic direction of the sample. The data is then plotted as a heat map [31] in polar coordinates with the radial axis being the parallel momentum transfer ΔK , the azimuthal axis being the orientation of the crystal α , and the color matching the logarithm of the detected intensity [33]. The resulting plots show the data where each colored patch is a data point with specular nominally in the center.

To demonstrate the method, a LiF crystal was cleaved along its (100) plane to form a $2 \times 2 \times 1 \text{ mm}$ sample, which was mounted on a sample stub and installed in the SHeM sample chamber ($\sim 10^{-8}$ mbar). The low reactivity of LiF enabled the sample to be cleaved *ex situ*, in air, with the subsequent mounting and installation taking a few minutes [26,34,35]. Diffraction measurements were collected at the locations marked in the overview SHeM

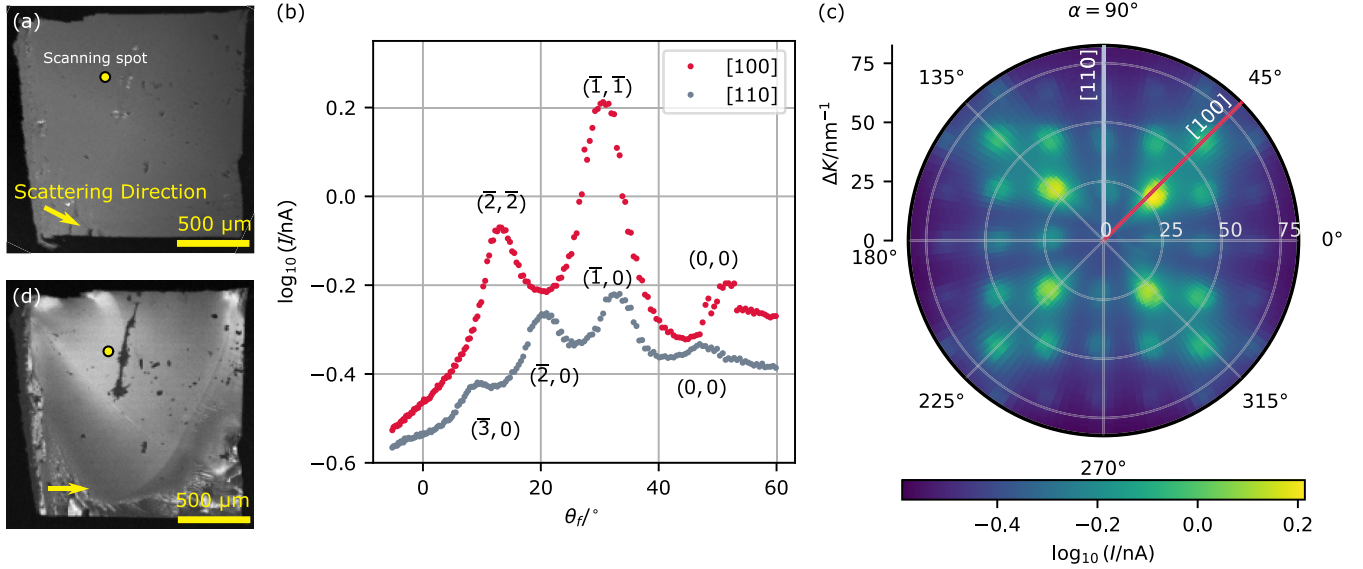


FIG. 2. (a) Helium micrograph of the cleaved LiF (100) surface, taken with the reciprocal-space detection condition far from any diffraction peak. A suitable measurement point was then chosen in the image, indicated by the yellow dot. A series of detection angle scans were taken on the spot at different azimuthal orientations; two examples are shown in (b), where diffraction peaks are clearly evident. By taking detection angle scans across the full 360° azimuthal range, the in-plane diffraction pattern shown in (c) was built up. All azimuthal directions were measured independently and are not repeated using knowledge of the lattice symmetry. The pattern was translated by $(5.5, 3.0) \text{ nm}^{-1}$ so that $\Delta K = 0$ corresponds to where the principle axes meet. The 2D diffraction pattern (c) obtained from the measurements clearly indicates the cubic arrangement of the LiF crystal, where the diffraction peaks observed along $\langle 110 \rangle$ have a lower intensity than those along $\langle 100 \rangle$. The first order peaks in these directions consistently have the highest respective intensities. (d) An image taken at the reciprocal-space detection condition corresponding to the strong $(\bar{1}\bar{1})$ diffraction peak, as indicated by the white point in panel (c). Because of the strongly varying scattering distribution at the new detection condition, contrast is significantly enhanced in (d) compared to (a), revealing variations in the cleaved surface.

micrographs shown in Figs. 2(a) and 2(d). Figure 2(b) shows detection angle scans along the [011] and [010] azimuths, where clear diffraction peaks are seen, highlighting the strength of these spatially resolved diffraction measurements. In contrast, conventional helium atom scattering (HAS) experiments average over a large surface area, and would therefore be degraded by the defects on the sample that are clearly evident in the SHeM micrograph, Fig. 2(d).

Figure 2(c) shows a complete 2D diffraction data set which was taken at the same point. The pattern was translated in 2D by $(5.5, 3.0) \text{ nm}^{-1}$ such that $\Delta K = 0$ corresponds to where the principle axes meet. In reciprocal space, the cubic lattice of the fluoride ions dominate the (100) surface, with the diffraction peaks along the [110] direction being particularly weak when compared to the others. By fitting a 2D Gaussian function and a second order polynomial background to each peak independently, a grid of reciprocal lattice points was found. The mean of the reciprocal lattice spacing \bar{G} was calculated along with the statistical standard error on the mean. The real-space lattice constant a can then be calculated

$$a = \frac{2\sqrt{2}\pi}{\bar{G}} = 407 \pm 5 \text{ pm}. \quad (2)$$

The value given for the error on a arises from statistical error and from the uncertainty in the magnitude of the incident wave vector in Eq. (1), which in turn arises from uncertainty in the temperature of the nozzle and from the finite parallel speed ratio of the helium beam [36]. Our measured lattice constant agrees with the accepted literature value to better than one standard deviation [37]. We also note the high level of precision and accuracy despite the relatively low angular resolution of our instrument, a result that arises from the large number of diffraction peaks we can observe natively through the full range of azimuthal angles. A more detailed description of the error calculation and of the fitting procedure is provided in Supplemental Material [24]. One notable feature of the diffraction data is the weak specular peak, which, although evident in the individual line scans in Fig. 2(b), is barely visible in Fig. 2(c). The effect is due to a combination of: small misalignments between the sample surface, the manipulator, and the rotation axis, the narrow angular width of the specular beam itself and from the intrinsically weak specular intensity relative to that of the other diffraction peaks [16,38]. As the sample rotates azimuthally, the specular transitions in and out of the optimal detection condition, resulting in the weak and variable specular signal that is observed. The effect is

amplified in the polar diffraction plot, as the data density around the center is highest. Further information and discussion of the sample misalignment is provided in Supplemental Material [24].

Having identified the location of diffraction peaks in reciprocal space, we can return to imaging of the sample either on, or away from, a diffraction peak. These configurations yield different modes of imaging, with some analogy to light and dark field microscopy. Two such images are presented in Fig. 2, with (d) being taken on one of the most intense diffraction peaks, thus enhancing contrast from small scale topographic changes, crystallographic misalignment, and defects. Figure 2(a) was taken away from a diffraction peak so that the contrast is smaller and largely comes from large scale topographic structure. The latter modality is consistent with typical SHeM imaging and produces micrographs similar to the diffuse topographic contrast seen routinely from technological samples [28].

We can now relate our microscale diffraction data to existing helium-surface potentials, thus both demonstrating consistency with large-area helium scattering and explaining the strong variation observed between diffraction peak intensities along $\langle 110 \rangle$ and $\langle 100 \rangle$ directions. There are several published He-LiF potentials, derived either from *ab initio* [39] or semiempirical [19,20] methods. Figure 3(a) shows a series of equipotential contours for the interaction potential reported by Celli *et al.* [19], although all have similar lateral averages and corrugation values. A combination of scattering calculations and ray tracing were used to synthetically generate the diffraction pattern that would be obtained from a surface with that potential in the SHeM instrument.

The close-coupling method [40] was used to determine the probability of helium atoms scattering with a particular surface-parallel momentum transfer, i.e., into a particular outgoing direction. The method involves expanding both the helium wave function and the surface potential as Fourier series, then coupling them through the Schrödinger equation. We used the iterative method of solution implemented by Manolopoulos and Wyatt [41] with up to 158 diffraction channels, both open and closed, and an integration range of $z = 1 \text{ \AA}$ to 17 \AA to achieve convergence. Angular distributions were generated at azimuthal increments of 1.25° . In house, Monte Carlo ray-tracing simulations [42,43] were then applied to generate SHeM detection angle scans, after adaption of the ray-tracing framework to accept numerically supplied scattering probability distributions. The simulation traces straight line paths of atoms as they scatter off the sample and local environment, matching the physical geometry of the instrument precisely. The simulated data was subsequently analyzed in the same way as the experimental measurements.

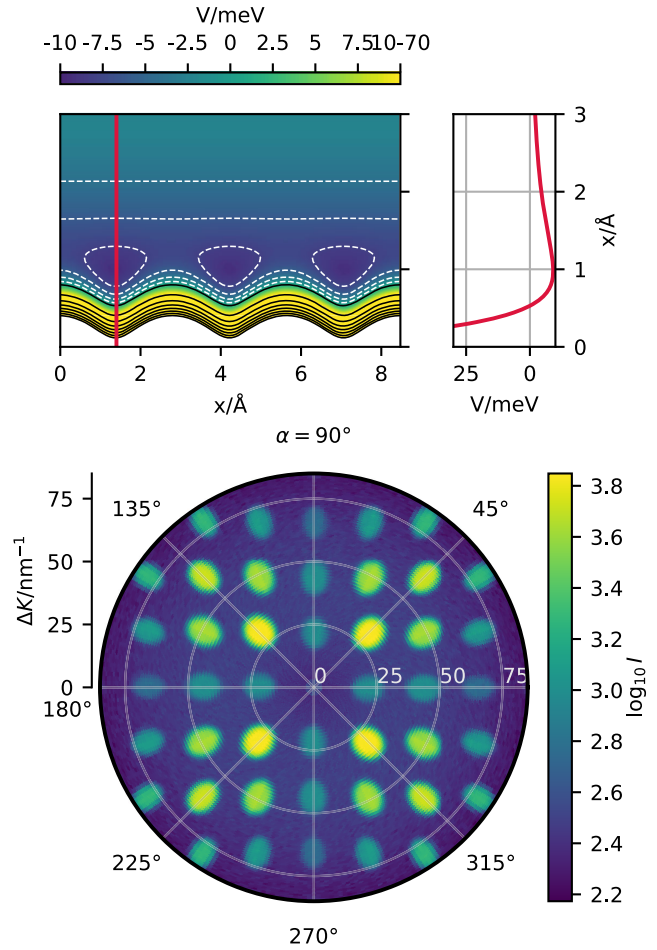


FIG. 3. (a) Contour plot along $[100]$ showing equipotential lines of the He-LiF potential from [19]. (b) 2D diffraction plot generated with the same method as Fig. 2(c), but using data calculated using a set of close-coupled equations predicting scattering probabilities, which were subsequently used in a ray-tracing framework to simulate scattered intensities from angular scans of He-LiF. The lower intensities of the diffraction peaks along $\langle 100 \rangle$ as compared to $\langle 110 \rangle$, are in agreement with the experimental data presented in Fig. 2(c).

Figure 3(b) shows the resulting synthetic helium diffraction pattern using the interaction potential reported by Celli *et al.* [19]. The location and intensity of the simulated diffraction peaks are in excellent qualitative agreement with the experimental data in Fig. 2(b), confirming that the intensity variation results from the local helium-surface potential, which in turn is well described by the model potential. Specifically, the low intensities along the $\langle 110 \rangle$ directions are replicated in the simulations, suggesting a high degree of out of plane scattering when compared to the $\langle 100 \rangle$ directions. There are small quantitative differences, such as with the second order $\langle 100 \rangle$ peaks; these differences are slightly increased if the potential from Celli *et al.* [19] is replaced with the potential from

Riley *et al.* [20]. However, the expected energy of the bound states is another important test of the quality of the potentials, with the potential from Riley *et al.* providing the more accurate prediction. Therefore, there is a deficiency of the current potentials, since neither can simultaneously predict both the bound state energies and the diffraction intensities accurately. Given that the bound state energies are relatively insensitive to the corrugation of the potential [20], while the opposite is true for the diffraction intensities, further work is needed where both of these aspects are simultaneously considered. However, in HAS it is usually more important to identify the presence and positions of peaks, and thus the orientation and symmetry of the surface lattice. Importantly, the ability to obtain microscale scattering data means helium diffraction can be applied to study a range of lattice properties, without the highly restrictive requirement of needing large single crystals.

In summary, we have demonstrated that SHeM can be exploited to measure diffraction from a micron-scale region of surface with only minor instrumental modifications. The resulting 2D diffraction pattern reveals the local lattice type, orientation, and size directly, and further quantitative analysis can be performed to relate the pattern to the underlying helium-surface potential. New imaging modalities have been demonstrated, made possible by recording scattered intensity at a particular condition in reciprocal space, enhancing surface features. Most importantly, the microscale diffraction opens up the possibility of applying established helium scattering methods to a vast new range of samples—the world beyond materials that can be grown into large single crystals. We expect the method to have a major impact on the ability to study small samples, such as 2D materials, where growth or exfoliation processes limit the sample size to the micron range, and polycrystalline materials where large single crystal domains are impractical. In the latter case, the demonstrated methods enable the identification and imaging of the grain structure directly, even in monolayer materials and with weakly bound adsorbate layers. The unique capabilities of helium scattering, such as the ability to measure electron-phonon coupling constants through diffraction [9], coupled with the microscale resolution through SHeM, suggest the technique will be highly profitable for addressing many experimental challenges in condensed matter to come.

A dataset supporting the presented work is published at [44].

The work was supported by EPSRC Grant No. EP/R008272/1. The authors acknowledge support by the Cambridge Atom Scattering Centre [45] and EPSRC Award No. EP/T00634X/1. The work was performed in

part at the Materials and NSW node of the Australian National Fabrication Facility, a company established under the National Collaborative Research Infrastructure Strategy to provide nano and microfabrication facilities for Australia’s researchers. S. M. L. acknowledges funding from MathWorks Ltd. B. L. acknowledges financial support from the CSC and the Cambridge Trust. We would also like to acknowledge constructive discussions with Bill Allison and Paul Dastoor.

Appendix A: Point tracking.—The calibration of rotational point tracking on a given sample surface can be performed by first taking SHeM images of an identifiable feature. In the current work, images of a corner of the LiF crystal were taken at periodic intervals around 360° of sample rotation. Figure 4 shows these SHeM images, which were plotted in the coordinate system of the sample manipulators. Assuming that the rotational axis is perpendicular to a completely flat sample, we expect the locus of the corner to trace out a circle. The center of rotation was obtained by fitting a circle to the set of points using the least squares method as implemented by Brown [46]. Once the center of rotation is known, any arbitrary point on the sample can be tracked by using a standard rotational transformation around the coordinates of the center of rotation.

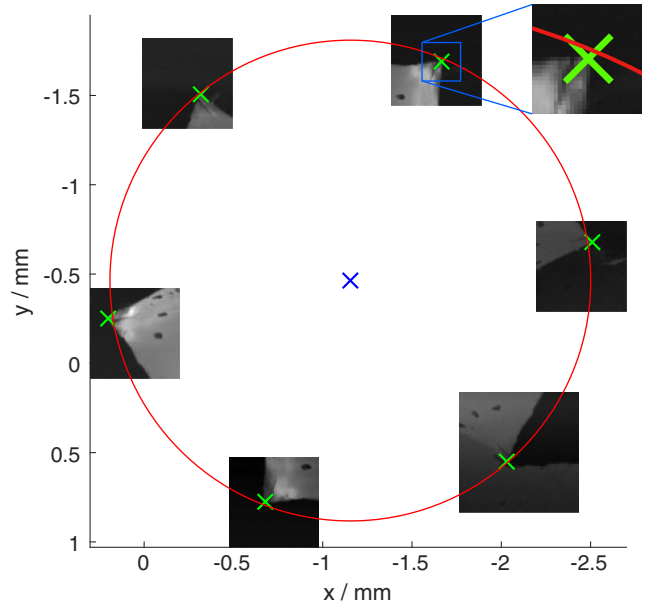


FIG. 4. Positions marked in green of the LiF sample’s tracked corner as it was rotated, with the fitted circle plotted in red and its center of rotation marked in blue. The maximum distance between the real positions of the corner and the fitted circle is $27\ \mu\text{m}$, with the inset demonstrating one of these deviations from the expected trajectory in more detail.

Appendix B: Beam properties.—The beam was formed from the supersonic expansion of helium at 100 bar from a 10 μm diameter nozzle at room temperature into the vacuum system. The incident helium beam energy was estimated to be 63.6 ± 0.7 meV, which corresponds to an incoming wave vector of magnitude 110.5 ± 0.5 nm⁻¹. The parallel speed ratio cannot be measured directly, however, given the source nozzle diameter and source pressure, we can interpolate a theoretical model by Toennies and Winkelmann [47] to predict the terminal parallel speed ratio to be ≈ 77 . The corresponding broadening of the first order diffraction peak is therefore expected to be $\sigma \sim 0.3^\circ$ and therefore will be negligible. Since the sample is at room temperature, we estimate that the diffraction peaks will be attenuated due to a Debye-Waller effect by a factor of $\sim 1/e$ [48], the remaining helium would then appear spread out across all other directions as a small background signal.

*Corresponding author: matthew.bergin@newcastle.edu.au

†Corresponding author: nav31@cam.ac.uk

‡These authors contributed equally to this work.

- [1] J. R. Schaibley, H. Yu, G. Clark, P. Rivera, J. S. Ross, K. L. Seyler, W. Yao, and X. Xu, Valleytronics in 2D materials, *Nat. Rev. Mater.* **1**, 16055 (2016).
- [2] D. Akinwande, C. J. Brennan, J. S. Bunch, P. Egberts, J. R. Felts, H. Gao, R. Huang, J. S. Kim, T. Li, Y. Li, K. M. Liechti, N. Lu, H. S. Park, E. J. Reed, P. Wang, B. I. Yakobson, T. Zhang, Y. W. Zhang, Y. Zhou, and Y. Zhu, A review on mechanics and mechanical properties of 2D materials—Graphene and beyond, *Extreme Mech. Lett.* **13**, 42 (2017).
- [3] N. R. Glavin, R. Rao, V. Varshney, E. Bianco, A. Apte, A. Roy, E. Ringe, and P. M. Ajayan, Emerging applications of elemental 2D materials, *Adv. Mater.* **32**, 1904302 (2020).
- [4] S. K. Tiwari, S. Sahoo, N. Wang, and A. Huczko, Graphene research and their outputs: Status and prospect, *J. Sci.* **5**, 10 (2020).
- [5] J. D. Caldwell, I. Aharonovich, G. Cassabois, J. H. Edgar, B. Gil, and D. N. Basov, Photonics with hexagonal boron nitride, *Nat. Rev. Mater.* **4**, 552 (2019).
- [6] S. Manzeli, D. Ovchinnikov, D. Pasquier, O. V. Yazyev, and A. Kis, 2D transition metal dichalcogenides, *Nat. Rev. Mater.* **2**, 1 (2017).
- [7] Y. Ma, Y. Dai, L. Kou, T. Frauenheim, and T. Heine, Robust two-dimensional topological insulators in methyl-functionalized bismuth, antimony, and lead bilayer films, *Nano Lett.* **15**, 1083 (2015).
- [8] D. Farias and K.-H. Rieder, Atomic beam diffraction from solid surfaces, *Rep. Prog. Phys.* **61**, 1575 (1998).
- [9] B. Holst, G. Alexandrowicz, N. Avidor, G. Benedek, G. Bracco, W. E. Ernst, D. Farias, A. P. Jardine, K. Lefmann, J. R. Manson, R. Marquardt, S. M. Artés, S. J. Sibener, J. W. Wells, A. Tamtögl, and W. Allison, Material properties particularly suited to be measured with helium scattering: Selected examples from 2D materials, van der Waals heterostructures, glassy materials, catalytic substrates, topological insulators and superconducting radio frequency materials, *Phys. Chem. Chem. Phys.* **23**, 7653 (2021).
- [10] P. Witham and E. Sánchez, A simple approach to neutral atom microscopy, *Rev. Sci. Instrum.* **82**, 103705 (2011).
- [11] M. Barr, A. Fahy, A. Jardine, J. Ellis, D. Ward, D. MacLaren, W. Allison, and P. Dastoor, A design for a pinhole scanning helium microscope, *Nucl. Instrum. Methods Phys. Res., Sect. B* **340**, 76 (2014).
- [12] D. A. Maclaren, B. Holst, D. J. Riley, and W. Allison, Focusing elements and design considerations for a scanning helium microscope (SHeM), *Surf. Rev. Lett.* **10**, 249 (2012).
- [13] M. Koch, S. Rehbein, G. Schmahl, T. Reisinger, G. Bracco, W. E. Ernst, and B. Holst, Imaging with neutral atoms—A new matter-wave microscope, *J. Microsc.* **229**, 1 (2008).
- [14] G. Bhardwaj, K. R. Sahoo, R. Sharma, P. Nath, and P. R. Shirhatti, Neutral-atom-scattering-based mapping of atomically thin layers, *Phys. Rev. A* **105**, 022828 (2022).
- [15] A. S. Palau, S. D. Eder, G. Bracco, and B. Holst, Neutral helium atom microscopy, *Ultramicroscopy* **251**, 113753 (2023).
- [16] G. Boato, P. Cantini, and L. Mattera, A study of the (001) LiF surface at 80 K by means of diffractive scattering of He and Ne atoms at thermal energies, *Surface Sci.* **55**, 141 (1976).
- [17] M. Debiassac, P. Pan, and P. Roncin, Grazing incidence fast atom diffraction, similarities and differences with thermal energy atom scattering (TEAS), *Phys. Chem. Chem. Phys.* **23**, 7615 (2021).
- [18] L. Danielson, J. C. R. Suarez, C. Schwartz, G. Scoles, and J. M. Hutson, Very low-energy scattering of helium atoms from crystal surfaces. A quantitative comparison between experiment and theory, *Faraday Discuss. Chem. Soc.* **80**, 47 (1985).
- [19] V. Celli, D. Eichenauer, A. Kaufhold, and J. P. Toennies, Pairwise additive semi *ab initio* potential for the elastic scattering of He atoms from the LiF(001) crystal surface, *J. Chem. Phys.* **83**, 2504 (1998).
- [20] D. J. Riley, A. P. Jardine, S. Dworski, G. Alexandrowicz, P. Fouquet, J. Ellis, and W. Allison, A refined He–LiF(001) potential from selective adsorption resonances measured with high-resolution helium spin-echo spectroscopy, *J. Chem. Phys.* **126**, 104702 (2007).
- [21] M. Bergin, D. J. Ward, S. M. Lambrick, N. A. von Jeinsen, B. Holst, J. Ellis, A. P. Jardine, and W. Allison, Low-energy electron ionization mass spectrometer for efficient detection of low mass species, *Rev. Sci. Instrum.* **92**, 073305 (2021).
- [22] Attocube Systems AG, ECSx3030/StSt/NUM+/UHV :: <http://www.attocube.com> (2023).
- [23] Attocube Systems AG, ECS Lift 3030/5050:: <http://www.attocube.com> (2023).
- [24] See Supplemental Material at <http://link.aps.org/supplemental/10.1103/PhysRevLett.131.236202> for sample manipulation, sample misalignment and peak identification.
- [25] Attocube Systems AG, ECR3030/StSt/NUM+/UHV:: <http://www.attocube.com> (2023).
- [26] M. Bergin, S. M. Lambrick, H. Sleath, D. J. Ward, J. Ellis, and A. P. Jardine, Observation of diffraction contrast in scanning helium microscopy, *Sci. Rep.* **10**, 2053 (2020).
- [27] M. Bergin, W. Roland-Batty, C. Hatchwell, T. Myles, J. Martens, A. Fahy, M. Barr, W. Belcher, and P. Dastoor,

- Standardizing resolution definition in scanning helium microscopy, *Ultramicroscopy* **233**, 113453 (2022).
- [28] S. Lambrick, The formation of contrast in scanning helium microscopy, Ph.D. thesis, University of Cambridge, Cambridge, 2022, [10.17863/CAM.83463](https://doi.org/10.17863/CAM.83463).
- [29] S. M. Lambrick, L. Vozdecký, M. Bergin, J. E. Halpin, D. A. MacLaren, P. C. Dastoor, S. A. Przyborski, A. P. Jardine, and D. J. Ward, Multiple scattering in scanning helium microscopy, *Appl. Phys. Lett.* **116**, 061601 (2020).
- [30] M. Bergin, T. A. Myles, A. Radić, C. J. Hatchwell, S. M. Lambrick, D. J. Ward, S. D. Eder, A. Fahy, M. Barr, and P. C. Dastoor, Complex optical elements for scanning helium microscopy through 3D printing, *J. Phys. D* **55**, 095305 (2021).
- [31] Using the `pcolormesh` from the `Matplotlib` module of PYTHON [32].
- [32] J. D. Hunter, Matplotlib: A 2D graphics environment, *Comput. Sci. Eng.* **9**, 90 (2007).
- [33] S. Lambrick, SHeM-diffraction-analysis: Release with final version of the LiF paper, [10.5281/ZENODO.8096928](https://doi.org/10.5281/ZENODO.8096928) (2023).
- [34] G. Armand, J. Lapujoulade, and Y. Lejay, The Debye-Waller factor in helium scattering by a crystalline surface, *Surface Sci.* **63**, 143 (1977).
- [35] J. C. Crews, Scattering of helium and argon from the cleavage plane of lithium fluoride, *J. Chem. Phys.* **37**, 2004 (1962).
- [36] G. Scoles, *Atomic and Molecular Beam Methods*, Atomic and Molecular Beam Methods, No. v. 1 (Oxford University Press, New York, 1988), <https://books.google.co.uk/books?id=4uJnAQAAAJ>.
- [37] D. R. Lide, *CRC Handbook of Chemistry and Physics* (CRC Press, Boca Raton, 1992), Vol. 72.
- [38] G. Brusdeylins, R. B. Doak, and J. P. Toennies, High-resolution helium time-of-flight studies of Rayleigh surface-phonon dispersion curves of LiF, NaF, and KCl, *Phys. Rev. B* **27**, 3662 (1983).
- [39] P. W. Fowler and J. M. Hutson, Pairwise-additive models for atom-surface interaction potentials: An *ab initio* study of He-LiF, *Phys. Rev. B* **33**, 3724 (1986).
- [40] G. Wolken, Collision of a diatomic molecule with a solid surface, *J. Chem. Phys.* **59**, 1159 (1973).
- [41] D. E. Manolopoulos, R. E. Wyatt, and D. C. Clary, Iterative solution in quantum scattering theory. The log derivative Kohn approach, *J. Chem. Soc., Faraday Trans.* **86**, 1641 (1990).
- [42] S. M. Lambrick, M. Bergin, A. P. Jardine, and D. J. Ward, A ray tracing method for predicting contrast in neutral atom beam imaging, *Micron* **113**, 61 (2018).
- [43] S. Lambrick and D. Sermet, SHeM-Ray-Tracing-Simulation: 2D helium atom diffraction from a microscopic spot (final version), [10.5281/ZENODO.8096928](https://doi.org/10.5281/ZENODO.8096928) (2023).
- [44] S. Lambrick, N. Von Jeinsen, M. Bergin, A. Radic, B. Liu, D. Sermet, A. Jardine, and D. Ward, Dataset supporting “2D helium atom diffraction from a microscopic spot,” Apollo—University of Cambridge Repository, [10.17863/CAM.99115](https://doi.org/10.17863/CAM.99115) (2023).
- [45] <https://atomscattering.phy.cam.ac.uk/>.
- [46] R. Brown, `fitcircle.m`—File Exchange—MATLAB Central.
- [47] J. P. Toennies and K. Winkelmann, Theoretical studies of highly expanded free jets: Influence of quantum effects and a realistic intermolecular potential, *J. Chem. Phys.* **66**, 3965 (1977).
- [48] G. Vidali and C. Hutchings, Measurement of the Debye-Waller factor for He-LiF(001), *Phys. Rev. B* **37**, 10374 (1988).